ELSEVIER

Journal of Fluids and Structures 19 (2004) 467–489

JOURNAL OF
FLUIDS AND
STRUCTURES

www.elsevier.nl/locate/jnlabr/yjfls

Numerical simulations of vortex-induced vibration on flexible cylinders

C.T. Yamamoto[a], J.R. Meneghini[b,*], F. Saltara[b], R.A. Fregonesi[b],
J.A. Ferrari Jr.[c]

[a] *Department of Naval Engineering, University of São Paulo, Brazil*
[b] *Department of Mechanical Engineering, EPUSP—University of São Paulo, AV. Prof. mello de Moraes, 2231 São Paulo, SP 05508-900, Brazil*
[c] *E&P, Petrobras, Rio de Janeiro, Brazil*

Received 26 July 2002; accepted 27 January 2004

Abstract

The main purpose of the research described in this paper is to investigate the hydroelastic interactions that take place between oscillating flexible cylinders and fluid forces. The cylinders are subject to currents and shear flow, and the hydrodynamic forces are estimated by a discrete vortex method. The calculations are compared with results obtained using the quasi-steady theory, as proposed by Bearman et al. (Appl. Ocean Res. 6(3) (1984) 166) and employed by Ferrari (Ph.D. Thesis, University of London, UK, 1998). In addition, the calculations are compared with experiments carried out by Fujarra (M.Sc. Thesis, Universidade de São Paulo, 1997) involving a cantilever flexible cylinder immersed in a current. The normalized amplitude curve obtained in the calculations is compared with the experimental results. Visualizations of the wake indicate a hybrid mode of vortex shedding along the span. Employing the terminology suggested by Williamson and Roshko (J. Fluids Struct. 2 (1988) 355), a 2S mode is found in regions of low amplitudes, changing to a 2P mode in regions of larger amplitudes. The position where transition of modes occurs varies with the reduced velocity. A practical case of a vertical marine riser is shown, and the numerical results for various current profiles are discussed.

1. Introduction

Risers are long flexible circular cylinders exposed to all sort of oceanographic conditions. They are used to link the seabed to the offshore platforms for oil production. Some of these floating platforms are installed along the continental shelf of the Atlantic Ocean where water depths over 1000 m are common. In such conditions, a better comprehension of the vortex dynamics causing vibration and fatigue of risers is essential.

With risers presenting such high aspect ratios and complex flow fields around them, a complete three-dimensional simulation at realistic conditions is unfeasible. With this in mind and aiming at the hydroelastic response of the riser structure, a numerical model in a quasi-three-dimensional fashion is developed in this paper. By a quasi-three-dimensional approach, we mean that the hydrodynamic forces are evaluated in two-dimensional strips, and the coupling between those strips occurs through a three-dimensional structural calculation. A finite element structural model based on the Euler–Bernoulli beam theory is developed in order to accomplish the task of integrating the hydrodynamic forces calculation and the dynamic response of the cylinder. A general equation of motion is solved

---

*Corresponding author. Tel.: +55-11-3091-5641; fax: +55-11-3091-5642.
E-mail address: julio.meneghini@poli.usp.br (J.R. Meneghini).

0889-9746/$ - see front matter © 2004 Elsevier Ltd. All rights reserved.
doi:10.1016/j.jfluidstructs.2004.01.004

through a numerical integration scheme in the time domain. The technique used for evaluating the hydrodynamic forces is the Discrete Vortex Method (DVM).

A practical case of a vertical marine riser is presented. In this case, the results for various uniform and shear currents acting on a single-flexible cylinder, representing a riser with a length equal to 120 m with 100 m under water, are shown. Envelopes of maximum and minimum in-line and transverse displacements are presented.

Our intention is to apply this model to problems occurring in the offshore industry. The risers are slender structures, which are subject to shear and oscillatory flows due to currents and waves, flows with a very high degree of complexity, with intensity and direction changing with the depth of water. We believe that the main contribution of this study is to integrate known methods in an innovative way. Building a practical CFD tool to investigate the hydroelastic problems shown in this paper is of great interest to the oil industry. The life span of the marine risers is significantly affected by vortex-induced vibration. The algorithm developed in this research is especially efficient in cases with very long risers. Besides, it is ideally suited to cases in which there is more than one riser in the flow. A forthcoming paper will present results related to this last situation. The results obtained here show the expected behaviour of a riser immersed in a uniform current, and a very good agreement with the quasi-steady theory in a shear flow case.

Recent investigations have focused on obtaining a reliable procedure to simulate vortex-induced vibration on long cylinders. Wildden and Graham (2001) employed a hybrid scheme to examine fluid–structure interaction on marine risers. The structural part of their scheme is similar to the one employed in our simulations. However, they used a vortex method with a hybrid formulation that required a mesh to evaluate the diffusion of vorticity. Even though their scheme is very accurate, it is more demanding from a computational point of view. A similar approach using a vortex method can be found in the work by Herfjord et al. (1999). The flow around an elastic cylinder with an aspect ratio of about 60 has also been studied by Wang et al. (2001) employing a finite element method. So et al. (2003) developed a mesh shape preservation technique to simulate two oscillating circular cylinders.

Other references that should be cited are the extensive work by Evangelinos et al. (2000) and Lucor et al. (2001). A spectral element method, as described by Karniadakis and Sherwin (1999), has been employed to study the flow–structure interaction. They utilized a fully three-dimensional code to investigate vortex-induced vibration. Their simulations were performed at low Reynolds numbers, and showed the applicability of this high-order method for fundamental studies.

Patel and Witz (1991) and Ferrari (1998) developed a structural model for a single riser based on the finite element technique applied to beam elements. Following Ferrari, a static model is used to obtain the solution for the eigenvalue problem and to evaluate the eigenfrequencies and the eigenmodes. With this approach, the nodes are free to rotate and to displace in the vertical, transverse and in-line directions.

The results presented in our investigation are based on the structural model explained briefly above. The hydrodynamic forces are assessed through the DVM, as developed and employed by Spalart et al. (1983), Park and Higuchi (1989) and Meneghini (1993). This method is a Lagrangian numerical scheme technique for simulating two-dimensional, incompressible and viscous fluid flow. It employs the stream function-based boundary integral method and incorporates the growing core size or core spread method in order to model the diffusion of vorticity. Other examples of utilization of the DVM can be seen in Smith and Stansby (1988) and Yeung et al. (1993). An extensive review about vortex methods can be found in Sarpkaya (1989).

This paper is divided into six sections. A description of the structural model is given in Section 2. Following that explanation, the hydrodynamic model employed in the calculations is shown and discussed in detail. Calculations for a flexible cantilever model are carried out and compared with the experimental results by Fujarra (1997). Then, the model is applied to a marine riser case and, in Section 5, comparisons with the quasi-steady theory are carried out. Finally, in Section 6, conclusions are drawn based on the results presented.

2. Structural model

In order to accomplish the task of integrating the hydrodynamic forces calculation and the dynamic response of the cylinder, a finite element structural model is developed, and shown in this section. A general equation of motion is solved through a numerical integration scheme in the time domain. This numerical structural model is based on the studies of Patel and Witz (1991) and Ferrari (1998).

A static solution of the riser is firstly obtained, and we shortly present the governing equations and their solutions. In the dynamic analysis, the stiffness matrix obtained from the static analysis is used as an average approximation, and then a lumped approach is employed. A mass lumped matrix is also constructed and the damping matrix is evaluated in a global manner.

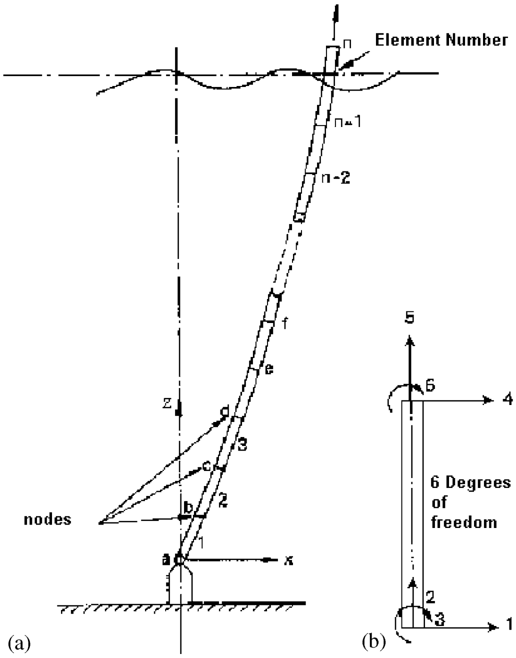

(a) (b)

Fig. 1. Degrees of freedom in an element, adapted from Patel and Witz (1991).

2.1. Governing equation for marine risers

A consistent static stiffness matrix is obtained through a finite element technique applied to an Euler–Bernoulli beam equation, and a truss bar equation. Each element has six degrees of freedom. Assuming small deflections of the beam, the Euler–Bernoulli equation can be derived from the equilibrium equations in a very small element. It has the following form:

$$\frac{d^2}{dz^2}\left(EI\frac{d^2\mathbf{x}}{dz^2}\right) - [T(y) + A_o p_o - A_i p_i]\frac{d^2\mathbf{x}}{dz^2} = \mathbf{f} + (\gamma_s A_s - \gamma_o A_o + \gamma_i A_i)\frac{d\mathbf{x}}{dz}, \tag{1}$$

where EI is the riser bending stiffness, T is axial tension in the riser pipe wall, and $\mathbf{f}$ is the force per unit length. With z measured from the bottom of the beam and positive upward, with $\mathbf{x}$ denoting the horizontal deflections from a vertical through the base. The external hydrostatic pressure is p_o; the internal hydrostatic pressure is p_i, with A_o being the cross-sectional area of the riser bore and wall, A_i the cross-sectional area of the riser bore only, A_s the cross-sectional area of wall, γ_i the specific weight of fluid in the riser bore, γ_o the specific weight of fluid surrounding the riser tube (sea water), and γ_s the specific weight of riser pipe wall material.

The axial degrees of freedom, indicated by indices 2 and 5 in Fig. 1, can be added in the elemental matrix of the structure, employing the finite element technique in a truss bar equation, yielding

$$EA\frac{d^2u(z)}{dz^2} = q, \tag{2}$$

where A is transverse area of the riser, u is the axial translation and q is the axial load. All six degrees of freedom are shown in Fig. 1. The Euler–Bernoulli beam equation gives the transverse degrees of freedom, 1 and 4, as well the rotations 3 and 6. The axial degrees of freedom, 2 and 5, are given through the truss bar equation.

2.2. Static and dynamic analysis

In order to find the static configuration of the riser, an incremental iterative procedure is adopted. This iterative procedure corrects the solution successively until equilibrium under a total load $\mathbf{F}$ is satisfied. Note that two linear systems are needed to describe the displacements of the riser, one to describe the in-line displacements, i.e. the free current direction; and another to describe the transverse displacements.

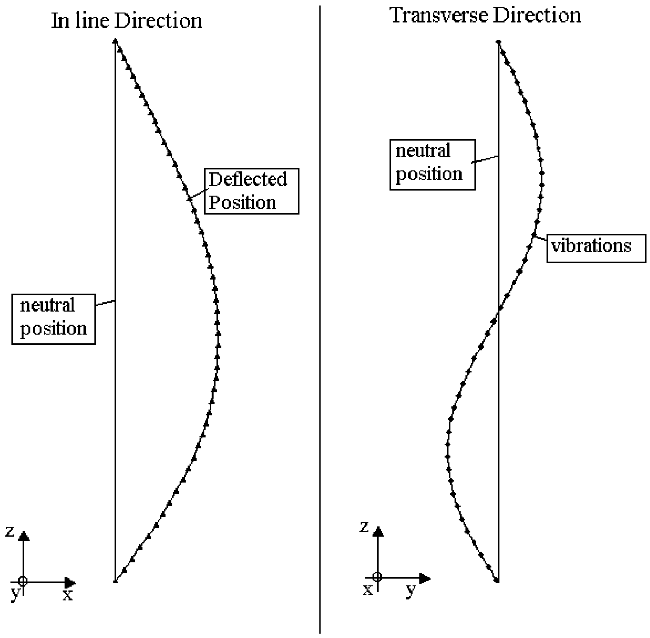

Fig. 2. Deflections/vibrations in in-line and transverse directions.

The static analysis is carried out only for the in-line configuration since it is the flow direction, and a deflected configuration is assumed. A deflected shape of the flexible cylinder is obtained. The stiffness matrix of the structure in its deformed position is available at the end of the static analysis. The dynamic response is assessed about this mean statically deflected shape. Fig. 2 shows both directions.

Comparisons between the solution of the finite element model and the analytical solution for a weightless vertical beam with constant flexural rigidity and under constant in-line load yielded a very good agreement. These comparisons can be seen in Ferrari (1998). This attests the correctness of the finite element algorithm employed here for the structural solution. A particular weighted residual approach, the weak formulation of the Galerkin method [see Zienkiewicz and Morgan (1983) for details] is employed. Applying the Galerkin method to the first term of Eq. (1) we obtain an elastic stiffness matrix, which is not dependent on the configuration of the structure. Also, applying the weak formulation to the truss bar equation (2), and combining with the matrices obtained from Eq. (1), we obtain a consistent global stiffness matrix, representing the elastic stiffness of the riser.

The elemental matrix for a vertical marine riser, derived from this procedure, has the following form:

$$\begin{bmatrix} \frac{EA}{L} & 0 & 0 & -\frac{EA}{L} & 0 & 0 \\ & \frac{12EI}{L^3} & \frac{6EI}{L^2} & 0 & \frac{-12EI}{L^3} & \frac{6EI}{L^2} \\ & & \frac{4EI}{L} & 0 & \frac{-6EI}{L^2} & \frac{2EI}{L} \\ & & & \frac{EA}{L} & 0 & 0 \\ & \text{sym} & & & \frac{12EI}{L^3} & \frac{-6EI}{L^2} \\ & & & & & \frac{4EI}{L} \end{bmatrix}. \tag{3}$$

The second term of Eq. (1) yields a geometric stiffness matrix, which is dependent on the configuration of the structure through the axial tension term. The elemental geometric stiffness matrix for a vertical marine riser has the following form:

$$\frac{(T+p_oA_o+p_iA_i)}{L}\begin{bmatrix} 0 & 0 & 0 & 0 & 0 & 0 \\ & \frac{6}{5} & \frac{L}{10} & 0 & \frac{-6}{5} & \frac{L}{10} \\ & & \frac{2L^2}{15} & 0 & \frac{-L}{10} & \frac{-L^2}{30} \\ & & & 0 & 0 & 0 \\ & \text{sym} & & & \frac{6}{5} & \frac{-L}{10} \\ & & & & & \frac{2L^2}{15} \end{bmatrix}. \tag{4}$$

Note that the elemental geometric stiffness matrix, Eq. (4), depends on the solution of our problem. The tension term T is the tension in the element axis direction, as can be seen in Fig. 3, and $T_z(z)$ is the vertical tension and it is assessed by the top tension less the self-weight of the riser,

$$T_z(z) = T_{\text{top}} - \gamma_s A_s (z_{\text{top}o} - z), \tag{5}$$

where T is the projection of $T_z(z)$ in the element axis; ϕ is the rotation of the riser, so it is the solution to the problem. The geometric stiffness matrix depends on the rotation of the riser.

Using Galerkin's method in the force terms of Eqs. (1) and (2), i.e. the right-hand side term, we obtain the basic equation for a rigid riser. The second term of Eq. (1) is treated as a load term, $\mathrm{d}\mathbf{x}/\mathrm{d}t$ is initially assumed as the undeflected riser configuration. The general form is

$$\mathbf{K}_E + \mathbf{K}_G(\mathbf{d})\mathbf{d} = \mathbf{F}, \tag{6}$$

where $\mathbf{K}_E$ denotes the elastic global stiffness matrix, $\mathbf{K}_G(\mathbf{d})$ is the geometric stiffness matrix, $\mathbf{d}$ is the displacement vector (solution), which is given by the two translations and one rotation for each node, and $\mathbf{F}$ is the force vector. In the proper coordinate system, $\mathbf{F}$ is given by the longitudinal forces (self-weight), transverse forces (drag and inertia forces due to the flow field), and bending moment.

An incremental iterative procedure is adopted with the intention of finding the static configuration of the riser, i.e. vector $\mathbf{d}$. This iterative procedure corrects the solution successively until equilibrium under a total load $\mathbf{F}$ is satisfied. One can note that two systems like Eq. (6) are needed, one to describe the in-line displacements, and another to describe the transverse deflections. The static analysis is carried out only for the in-line configuration, since it is the flow direction, and a deflected configuration is assumed. A deflected shape of the flexible cylinder is obtained, and, at the end of the static analysis, the stiffness matrix of the structure in its deformed position is calculated. The dynamic response is assessed about this mean statically deflected shape. Comparisons between the solution of the finite element model and the analytical solution, for a weightless vertical beam with constant flexural rigidity and under constant in-line load, provided a very good agreement, which attests to the correctness of the finite element formulation.

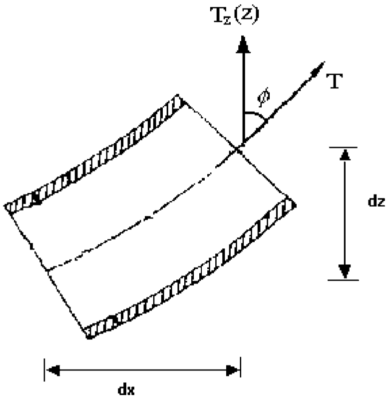

Fig. 3. Tension term in an element.

Since the hydrodynamic forces are assessed through two-dimensional strips of the flow, vertical forces are not included in the calculations. So, in order to have a simplified definition of element properties and a more efficient computational code, the dynamic model uses a lumped approach.

The differential equation of motion for a system with many degrees of freedom can be written as

$$\mathbf{M}\ddot{\mathbf{d}} + \mathbf{B}\dot{\mathbf{d}} + \mathbf{K}\mathbf{d} = \mathbf{F}, \tag{7}$$

where $\mathbf{d}$ is the vector of nodal displacements; $\mathbf{M}$, $\mathbf{B}$, $\mathbf{K}$ are the mass, structural damping and stiffness matrix respectively; and $\mathbf{F}$ is the force vector.

The force vector $\mathbf{F}$ is obtained from two-dimensional calculations employing the Discrete Vortex Method (DVM), which will be presented in the next section. The mass matrix assumes that the mass is concentrated at the end of the nodes. With this approach, the mass matrix has a diagonal form. Off-diagonal terms disappear since the acceleration of any nodal point would only produce an inertia force at that point. The elemental mass matrix has the following form:

$$\begin{bmatrix} \frac{1}{2}(\rho_s A_s + \rho_i A_i)L & 0 \\ 0 & \frac{1}{2}(\rho_s A_s + \rho_i A_i)L \end{bmatrix}, \tag{8}$$

where ρ_s and ρ_i are the density of the material of the pipe wall and the density of the fluid in the riser bore.

The lumped stiffness matrix is obtained by isolating the horizontal degrees of freedom of the consistent stiffness matrix from others. In the lumped approach, all rotational degrees of freedom need to be subtracted. The vertical translational degrees of freedom are also eliminated. This feature can lead to a substantial reduction in computer time and storage in the dynamic analysis. The lumped stiffness matrix can be derived from the consistent stiffness matrix segregating the horizontal degrees of freedom from other displacements, the force equation can be written in partitioned form as

$$\begin{bmatrix} \mathbf{K}_{HH} & \mathbf{K}_{HVR} \\ \mathbf{K}_{VRH} & \mathbf{K}_{VV} \end{bmatrix} \begin{Bmatrix} \mathbf{D}_H \\ \mathbf{D}_{VR} \end{Bmatrix} = \begin{Bmatrix} \mathbf{F}_H \\ \mathbf{0} \end{Bmatrix}, \tag{9}$$

where the subscripts H, V and R denote the horizontal, vertical and rotational degrees of freedom, respectively (e.g. $\mathbf{K}_{HH}$ represents the horizontal degrees of freedom in the consistent stiffness matrix).

The condensed or reduced stiffness matrix, suitable for use in the equations of motion, derived from Eq. (9) is

$$\mathbf{K}_{\text{lumped}} = \mathbf{K}_{HH} - \mathbf{K}_{HVR}\mathbf{K}_{VV}^{-1}\mathbf{K}_{VRH}. \tag{10}$$

At the end of the static analysis, the stiffness matrix of the structure in its deformed position is available. In modelling the dynamic response about this mean statically deflected shape, the stiffness matrix is assumed to remain constant throughout the dynamic analysis.

The definition of the structural damping, considering the damping of the pipe material and the friction of the joints, is a difficult and imprecise task. In this work, the structural damping is defined in a global manner, considering the whole system as the sum of the individual material properties.

The structural damping matrix is assessed through the Proportional Rayleigh Damping method. It may be defined as

$$\mathbf{B} = a_0\mathbf{M} + a_1\mathbf{K}. \tag{11}$$

$\mathbf{B}$, in Eq. (11), is the damping structural matrix, and is proportional to the mass and stiffness matrix; a_0 and a_1 are coefficients that are functions of two eigenvalues, and two respective damping ratios; for more details see Craig (1981).

An eigenvalue analysis is carried out to find the natural frequencies corresponding to the two modes chosen. Following Ferrari (1998), a reasonable approximation for the natural frequencies of a rigid vertical riser can be given through the analytical solution of a beam in natural vibration, with constant cross-section and subject at the ends to axial tensile forces. The natural frequencies can also be adjusted to simulate the real behaviour of a marine riser. This equation provide results in a very good agreement (error $<5\%$), when compared to the numerical solution of eigenvalue problem using the consistent approach.

Damping ratios (ζ) between 2% and 5% in the first two modes is usually chosen for the analyses of a marine riser. Although the actual level of structural damping that should be specified is rather unclear in current literature. In the present work, Eq. (7) is solved through direct numerical integration in order to give the horizontal displacements. The method employed is the mean average acceleration method.

3. Hydrodynamic model

The DVM is a Lagrangian numerical scheme technique for simulating two-dimensional, incompressible and viscous fluid flow. The method employs the stream function-based boundary integral method and incorporates the growing core size or core spread method in order to model the diffusion of vorticity. The body wall is discretized in N_w panels, and N_w discrete vortices with circulation Γ_i are created from a certain distance from the wall, one for each panel. These vortices are convected and their velocities are assessed through the sum of the free-stream velocity and the induced velocity from the other vortices. The induced velocities are calculated through the Biot–Savart law.

Since N_w vortices are created at each time step, the number of vortices N_v in the computation grows rapidly. Then, it is necessary to use some procedure to keep the number of vortices under control. Otherwise, a longer simulation would become unfeasible, mainly due to the number of calculations to evaluate the induced velocities through the Biot–Savart law. The scheme employed is an amalgamation procedure.

The vorticity transport equation for an incompressible Newtonian fluid with an isotropic viscosity, and the stream function-vorticity equation can be written as

$$\frac{\mathrm{D}\omega}{\mathrm{D}t} = \nu\nabla^2\omega, \tag{12}$$

$$\nabla^2\psi = -\omega. \tag{13}$$

Eq. (13) can be written for each discrete vortex as

$$\nabla^2\psi_i = -\omega_i. \tag{14}$$

The induced velocity of each vortex can be obtained from the Biot–Savart law. To avoid the discontinuous distribution of induced velocity by a point vortex, Spalart et al. (1983) employed a rigid vortex particle, or "blob vortex", with a radius σ. The velocity induced by the vortex is given by

$$U_\theta = \frac{\Gamma}{2\pi}\frac{r}{r^2+\sigma^2}. \tag{15}$$

The vortices are created at a distance σ_0 from the body surface. This parameter is considered as the initial vortex core radius. From potential theory and considering expression (15), it is known that the stream function at a wall point i on the body wall due to a vortex distribution with N_v vortices each with strength Γ_j, a free vortex distribution with N_v vortices each with strength Γ_k (representing the wake), and free-stream velocity components U and V, is given by

$$\psi_i = \mathscr{I}m[Z_{w_i}(U-iV)] - \frac{1}{4\pi}\sum_{j=1}^{N_w}\Gamma_j \ln(|Z_{w_i}-Z_{c_j}|^2+\sigma_0^2) - \frac{1}{4\pi}\sum_{k=1}^{N_v}\Gamma_k \ln(|Z_{w_i}-Z_k|^2+\sigma^2) \tag{16}$$

for $1 \leqslant i \leqslant N_w$, where Z_{w_i} represents the complex coordinate of the control point i on the wall, Z_{c_i} is the coordinate of the j vortex created around the body, and Z_k is the coordinate of the k vortex located in the wake.

Similarly, the stream function at the wall point "i+1" is obtained just replacing the subscript "i" by "i+1", and since the body is a streamline, we can write

$$\psi_{i+1} - \psi_i = -\mathbf{V}_{\text{body}} \cdot \mathbf{n}\Delta S, \tag{17}$$

where $\mathbf{V}_{\text{body}}$ denotes the velocity and ΔS the size of the panel. Expression (17) yields a set of linear equations in the form

$$\mathbf{A\Gamma} = \mathbf{b}, \tag{18}$$

in which

$$\mathbf{A} \equiv a_{ij} = \frac{1}{4\pi}\ln\frac{|Z_{w_{i+1}}-Z_{c_j}|^2+\sigma^2}{|Z_{w_i}-Z_{c_j}|^2+\sigma^2}, \tag{19}$$

$$\mathbf{b} \equiv b_i = \mathscr{I}m\{(Z_{w_{i+1}}-Z_{w_i})((U-U_{\text{body}})-i(V-V_{\text{body}}))\} - \frac{1}{4\pi}\sum_{k=1}^{Nv}\Gamma_k \ln\frac{|Z_{w_{i+1}}-Z_k|^2+\sigma^2}{|Z_{w_i}-Z_k|^2+\sigma^2} \tag{20}$$

and $\mathbf{A}$ is determined by the body geometry and vortex creation points, $\mathbf{\Gamma}$ is the vector containing values of the circulation of the bound vortices (solution) and $\mathbf{b}$ is known from the free-stream velocity, circulations and positions of free vortices, and is recalculated at each time step.

With the purpose of conserving the total circulation, Kelvin's theorem is enforced on the linear system, expression (18). This is equivalent to imposing

$$\sum_{i=1}^{N_w} \Gamma_i = \sum_{k=1}^{N_{\text{vlost}}} \Gamma_k. \tag{21}$$

When a vortex hits the body, it is removed from the computation. The right-hand side of Eq. (21) is the same as the sum of lost circulation, thus the lost vortices are recreated by Kelvin's theorem. When more than one body is in the fluid, this equation is written for each body separately.

The core spread method uses the vortex core σ to model the diffusion of vorticity. The core size in Eq. (15) is substituted by a new core size at each time step. The rate at which the core size grows can be calculated as follows. First, the analytical solution of a diffusing vortex core is considered

$$U_\theta = \frac{\Gamma}{2\pi r}(1 - \mathrm{e}^{\,r^2/4\nu t}). \tag{22}$$

Due to computational reasons, instead of using Eq. (22), Park and Higuchi (1989) used a growing core size where the core radius was the position of the maximum value of velocity calculated by expression (22), which yielded

$$\sigma_o = 2.224\sqrt{\nu t}. \tag{23}$$

This equation can be written as

$$(\sigma^{n+1})^2 = (\sigma^n)^2 + 4.946\nu\Delta t, \tag{24}$$

where n denotes the time step, and ν is the kinematic viscosity of the fluid. Thus, the induced velocity is assessed with a growing vortex core, which models the diffusion of vorticity. Note that when a discrete vortex is moving away from the body, the core grows, and the induced velocity around it decreases.

Vortices are convected by the sum of the free stream and the induced velocity by all other vortices. The new positions of the already existing vortices are calculated employing a Lagrangian scheme

$$X_i^{n+1} = X_i^n + U_i^n \Delta t. \tag{25}$$

Since N_w vortices are created at each time step, the total number of vortices increases rapidly. As previously mentioned, the presence of too many vortices would make the computation unfeasible. With the intention of avoiding this, Spalart et al. (1983) employed a merging scheme if two vortices satisfy the following condition:

$$\frac{|\Gamma_i \Gamma_j|}{|\Gamma_i + \Gamma_j|} \frac{|Z_i - Z_j|^2}{(D_0 + d_i)^{1.5}(D_0 + d_j)^{1.5}} < V_0, \tag{26}$$

D_0 and V_0 are the merging and tolerance parameters. D_0 is used to control resolution near the body. The merging tolerance, V_0, preserves the desirable total number of vortices, N_v. The resulting amalgamated vortex is located at a position that satisfies the first moment of the distribution, i.e. at

$$Z = \frac{Z_i \Gamma_i + Z_j \Gamma_j}{\Gamma_i + \Gamma_j}, \tag{27}$$

with a vortex strength

$$\Gamma = \Gamma_i + \Gamma_j. \tag{28}$$

Drag and lift forces are calculated from direct integration of the pressure field and skin friction around the body. The total force, $\mathbf{F}_{\text{total}}$ is given by

$$\mathbf{F}_{\text{total}} = \mathbf{F}_{\text{pressure}} + \mathbf{F}_{\text{skin}}. \tag{29}$$

A particular form of Kelvin's theorem, valid for viscous flow, is employed with the purpose of evaluating the pressure contribution to the total force. If one considers the definition of circulation, and a Lagrangian approach for the acceleration of material particles, we find

$$\frac{\mathrm{d}\Gamma}{\mathrm{d}t} = \frac{\mathrm{d}}{\mathrm{d}t}\oint_C \mathbf{V}\cdot \mathrm{d}\mathbf{r} = \oint_C \frac{\mathrm{d}\mathbf{V}}{\mathrm{d}t}\cdot \mathrm{d}\mathbf{r}. \tag{30}$$

The Navier–Stokes equations are evoked for the total velocity derivative, yielding

$$\frac{\mathrm{d}\Gamma}{\mathrm{d}t} = -\oint_C \nabla \mathbf{p} \times \mathrm{d}\mathbf{r} + \nu \oint_C \nabla^2 \mathbf{V} \times \mathrm{d}\mathbf{r} = \nu \oint_S \nabla^2 \mathbf{V} \times \mathrm{d}\mathbf{r}. \tag{31}$$

In this expression, the pressure integral is zero as it is evaluated in a closed contour around the body. The last term of Eq. (31) can be expressed in terms of the normal derivative of the vorticity at the wall, yielding Kelvin's theorem for viscous flow

$$\frac{\mathrm{d}\Gamma}{\mathrm{d}t} = \nu \oint_S \left[\frac{\partial}{\partial s}\left(\frac{\partial V_s}{\partial s}\right) + \frac{\partial}{\partial n}\left(\frac{\partial V_s}{\partial n}\right)\right] \mathrm{d}S = \nu \oint_S \left[\frac{\partial}{\partial n}\left(-\frac{\partial V_n}{\partial s} + \frac{\partial V_s}{\partial n}\right)\right] \mathrm{d}S = \nu \oint_S \frac{\partial \omega}{\partial n} \mathrm{d}S. \tag{32}$$

This expression is rewritten in a discrete form as

$$\frac{\Delta\Gamma}{\Delta t} = \nu \left.\frac{\partial \omega}{\partial n}\right|_{\text{wall}} \Delta S, \tag{33}$$

in which $\Delta\Gamma$ is the net circulation generated in a given panel. The relationship between the circulation and the pressure is obtained employing once again the Navier–Stokes equations. At the wall, for a moving cylinder

$$\rho \mathbf{a}_{\text{body}} \cdot \mathbf{e}_s = -\frac{\partial p}{\partial s} - \rho \nu \frac{\partial \omega}{\partial n}, \tag{34}$$

where $\mathbf{a}_{\text{body}} \cdot \mathbf{e}_s$ is the body acceleration projected in the wall-tangent direction (s).

Rearranging this expression, and employing Eq. (31) we have

$$\frac{\partial p}{\partial s} = -\rho \frac{\Delta\Gamma}{\Delta t} \frac{1}{\Delta S} - \rho \mathbf{a}_{\text{body}} \cdot \mathbf{e}_s. \tag{35}$$

Now, the contribution to the pressure distribution from the circulation is referred as p^A and from the body acceleration as p^B, the pressure is evaluated in a given panel i by the following equation:

$$p_i^A = p_0^A - \frac{\rho}{\Delta t} \sum_{j=1}^{i} \Delta\Gamma_j. \tag{36}$$

In this expression, p_0^A is a reference pressure and can be made equal to zero. The term due to the body acceleration can also be integrated along the cylinder wall. Doing so, the total pressure force is then calculated by

$$\mathbf{F}_{\text{pressure}} = -\oint_S p \mathbf{e}_n \,\mathrm{d}S = -\oint_S (p^A + p^B) \mathbf{e}_n \,\mathrm{d}S = -\sum_{i=1}^{N_w} p_i^A \Delta S_i \mathbf{e}_{n_i} + \rho \pi R^2 (a_x \mathbf{e}_x + a_y \mathbf{e}_y). \tag{37}$$

Finally, the skin friction contribution is obtained from the definition of shear stress at the wall, and the definition of vorticity, which yields

$$\boldsymbol{\tau}_w = \mu \frac{\partial V_s}{\partial n} \mathbf{e}_s, \tag{38}$$

where $\boldsymbol{\tau}_w$ is the shear stress at the wall, and μ is the dynamic viscosity. In order to evaluate the normal derivative, a linear variation of the velocity is assumed close to a vortex panel yielding

$$\boldsymbol{\tau}_w = \mu \frac{V_s}{2\sigma_0} \mathbf{e}_s. \tag{39}$$

In this expression, σ_0 is the initial core, which corresponds to the normal distance from the newly created vortices to the cylinder wall. The skin friction contribution to the total force is obtained integrating Eq. (39),

$$\mathbf{F}_{\text{skin}} = \int_S \boldsymbol{\tau}_w \,\mathrm{d}S = \sum_{i=1}^{N_w} \mu \frac{V_{s_i}}{2\sigma_{0_i}} \Delta S_i \mathbf{e}_{s_i}. \tag{40}$$

After considering the contributions from skin friction and pressure, the force components are resolved in the two directions x,y, yielding F_x and F_y. These forces are then nondimensionalized as follows:

$$C_d = \frac{2F_x}{\rho U^2 D}, \tag{41}$$

$$C_l = \frac{2F_y}{\rho U^2 D}, \tag{42}$$

where D is the diameter of the circular cylinder.

4. Calculations

4.1. Results for a flexible cantilever model

In this section, comparisons of the calculations employing the code described above with experiments by Fujarra (1997) are carried out. Fujarra studied the amplitudes of vibrations due to vortex shedding in the flow around a flexible cantilever cylinder. In Fig. 4, a schematic view of his model is shown. The cylinder is clamped at one end, and free to move and rotate at the other extremity. Fujarra obtained the nondimensional amplitude versus reduced velocity curve. The numerical simulations in the quasi three-dimensional fashion are carried out in order to reproduce his results.

The discrete vortex method was first validated by a series of calculations reported by Meneghini (1993), Yamamoto (2002), and Fregonesi (2002). The prediction of Strouhal number and force coefficients are in good agreement with experiments: for the flow around a fixed circular cylinder, $\mathrm{Re}=10^4$, the Strouhal number obtained was $\mathrm{St}=0.19$, and the drag coefficient C_d=1.28. These results compare well with values found in the literature. In all calculations presented in this paper, 64 panels were employed to discretize the cylinder wall, and a nondimensional time step, Ut/D, equal to 0.01 has been used. The chosen parameters followed a convergence study presented by Yamamoto (2002).

The characteristics of the flexible cantilever are given in Table 1. Before comparing the numerical simulations with the experimental results, a set of calculations are carried out to check the numerical resolution and convergence of the structural part of the computational code. The cantilever is discretized in 10, 30, and 60 structural elements. The amplitude envelopes are compared for a reduced velocity, V_r, equal to 6.0. The reduced velocity is defined as

$$V_r = \frac{UT_1}{D}, \tag{43}$$

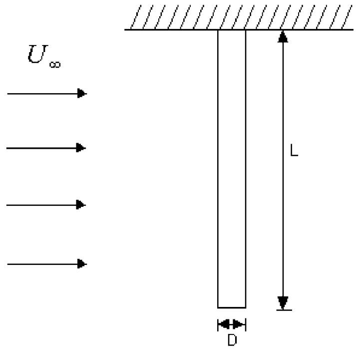

Fig. 4. Cantilever of length L and diameter D.

Table 1
Flexible cantilever model characteristics

Diameter, D	0.03175 m
Length, L	3.0 m
$(EI)_{eq}$	2658.4 N m^2
1st mode, structural damping measured in air, $\xi^s_{1\mathrm{ar}}$	0.57%
1st mode, natural frequency in air, $f_{1\mathrm{ar}}$	2.313 Hz
2nd mode, natural frequency in air, $f_{2\mathrm{ar}}$	15.832
Total system mass, m_{sys}	1.868 kg/m

where U is the free-stream velocity, and T_1 is the first mode period. As we can see in Fig. 5, the amplitudes seem to converge for a number of elements above 30. For this reason, and with the intention of having a proper numerical accuracy, a number of 60 elements have been chosen for all other simulations of the flexible cantilever cylinder.

Simulations have been carried out for values of reduced velocity varying from 3.0 to 20.0 with the purpose of obtaining the response amplitudes of oscillation. These velocities correspond to Reynolds numbers, Re, in the range $7000 \leqslant \mathrm{Re} \leqslant 47{,}000$. The numerical and experimental results are compared in Fig. 6. The cantilever amplitudes are

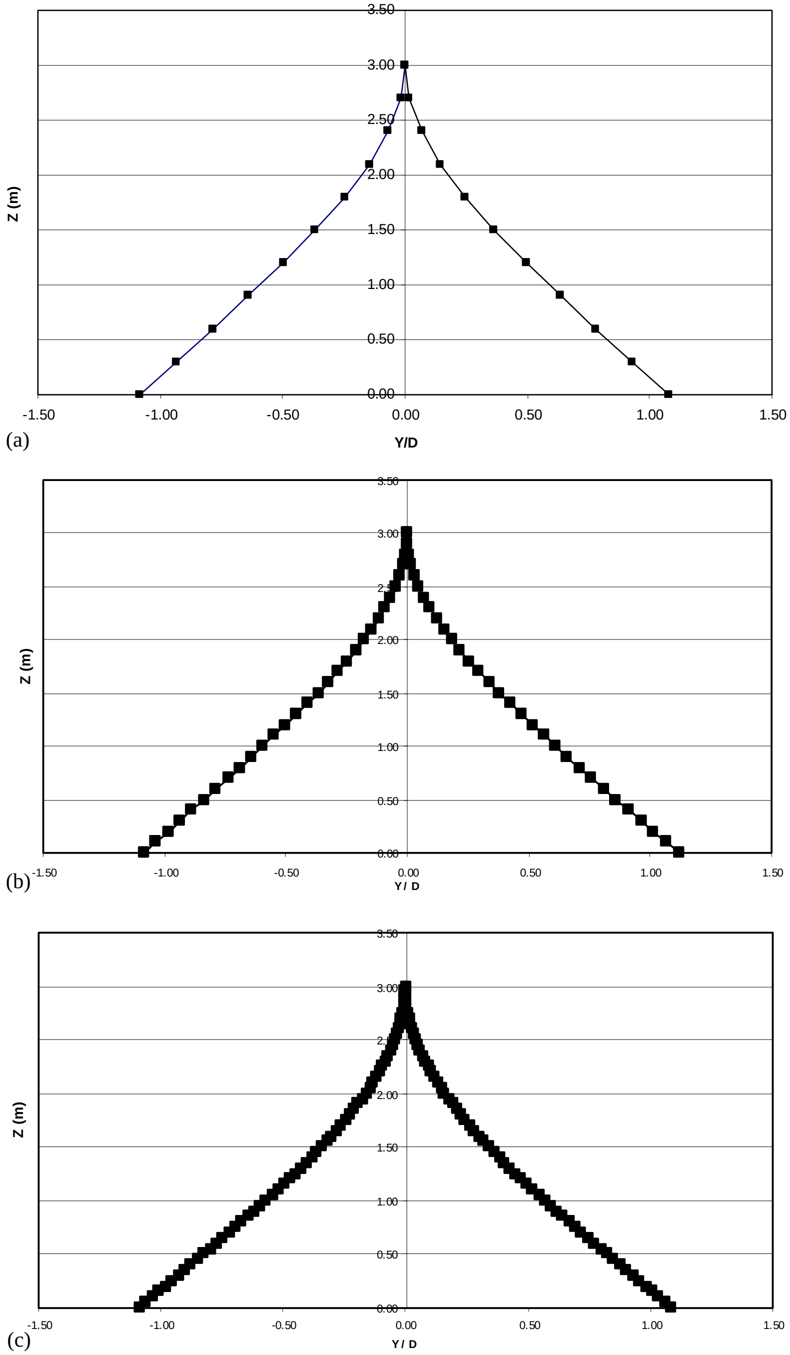

Fig. 5. Flexible cantilever cylinder, discretized with (a) 10 elements, (b) 30 elements, and (c) 60 elements. Maximum transverse amplitude, $V_r = 6.0$.

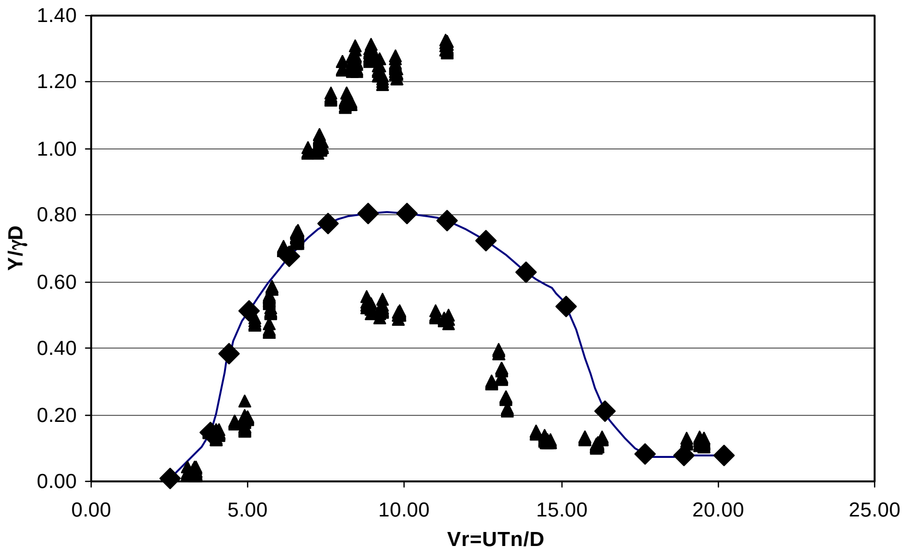

Fig. 6. Comparison of numerical calculations (——◆——) and experimental results obtained by Fujarra (1997) of an oscillating cantilever cylinder (▲).

normalized using an eigenmode factor γ, as explained in Fujarra et al. (2001). The structure vibrates in the first mode for all reduced velocities. In this case, $\gamma = 1.305$, and the normalized amplitude is $Y/\gamma D$.

As can be observed in Fig. 6, a very good agreement is obtained in part of the lock-in region. Our calculations yield amplitudes between the upper and lower branch in the region of maximum amplitudes. The maximum value of normalized amplitude obtained in the simulations is about 0.8. Although hysterisis has been observed in the experiments, the calculations have not shown this phenomenon.

Fig. 7 shows a wake visualization of the flow at the reduced velocity $V_r = 5$. The strips are plotted separately, section $Z = 0.0$ corresponds to the bottom strip, Z increases upward. A hybrid mode is observed along the oscillating cylinder. There is a transition from a 2S mode, close to the top, to a 2P mode near the bottom around the section $Z = 5.0$. The wake visualization of the flow at the reduced velocity $V_r = 9$ is shown in Fig. 8. Also, for this case, there is a transition from a 2S mode to a 2P mode. The dependency of this transition point with the reduced velocity is clearly observed. At $V_r = 9$, the transition occurs at section $Z = 15.0$.

It is interesting to compare these results with those obtained by Techet et al. (1998). They experimentally studied the flow around a tapered cylinder. The experiments were taken at different reduced velocities, Reynolds numbers and average diameters. In some cases, a hybrid mode was observed. A 2S pattern, along the region that experienced lower amplitudes, and a 2P pattern, along the region that experienced greater amplitudes, is observed. Fig. 9 shows schematically the hybrid mode proposed by them. They observed that this mode is periodic, differently from vortex bifurcations, and vortex dislocations. The location of the transition is stable and persistent when the experiments are repeated. They observed that the two patterns are phase locked and have the same frequency in the region of transition from mode 2S to 2P. There are no jumps in the phase angle inside this region.

In the cantilever model investigated in the present study, the dependency of the vortex shedding pattern with the nondimensional amplitude and the reduced velocity has also been observed. The two patterns are phase locked and have the same frequency in the transition region. Fig. 10 shows the phase between the lift coefficient and the displacement. It can be seen that where the transition between the two modes occurs, at around $Z = 5.0$, there is no abrupt jump in the phase value. Furthermore, we can observe that the phase changes its signal at this location.

4.2. Results for a single marine riser

Some results of a marine riser simulation are presented in this section. The riser has the following characteristics: water depth = 100 m, riser length = 120 m, riser pipe outside diameter = 0.25 m, riser pipe inside diameter = 0.2116 m, top tension = 200 kN (~1.5 times the riser self-weight), modulus of elasticity of riser pipe = 210,000,000.0 kN/m^2, specific weight of the fluid surrounding the riser = 1025 kg/m^3, specific weight of the fluid in the riser bore = 800 kg/m^3, specific weight of the riser wall material = 7700 kg/m^3.

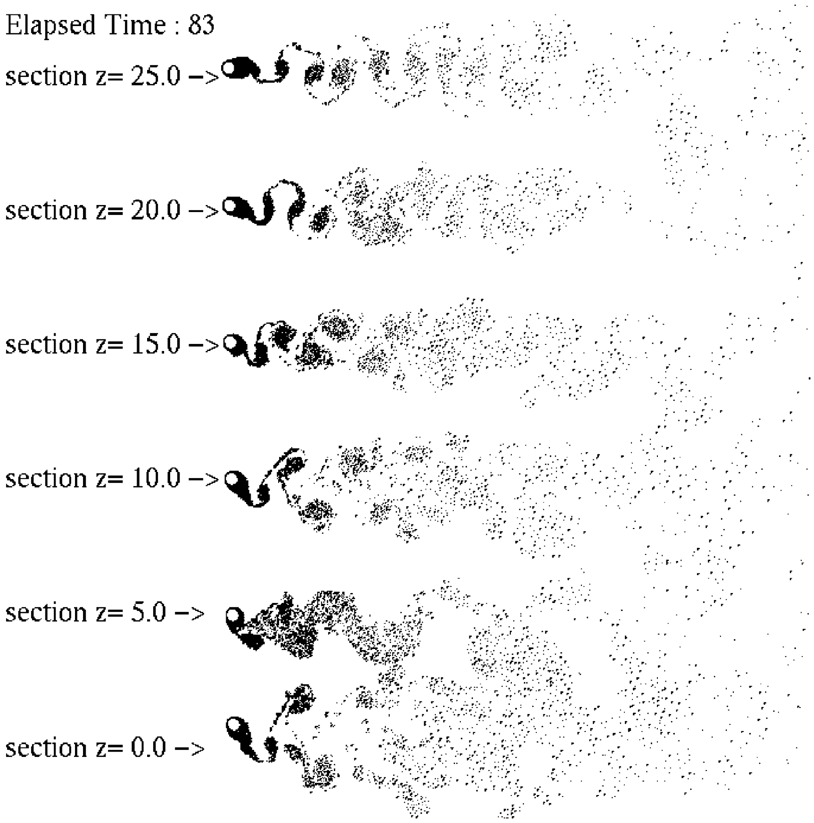

Fig. 7. Wake visualization—reduced velocity $V_r = 5$.

The riser is modelled with 40 elements equally spaced below the still water level (40 hydrodynamic sections), and 10 elements equally spaced above the water level. The riser is subjected to uniform flow, and the simulations were carried out at current velocities varying from 0.16 to 0.93 m/s. These currents correspond to Reynolds numbers in the range $4.0 \times 10^4 \leqslant \mathrm{Re} \leqslant 2.3 \times 10^5$. The riser has its extremities fixed but free to rotate.

The envelopes of transverse displacements and the power spectra for currents 0.23, 0.38, 0.54, and 0.85 m/s are shown in Figs. 11–17. The mode of transverse vibration changes increasing the current velocity, as can be observed in those figures. The analysis of those envelopes gives an indication in which mode the structure is vibrating. Analysing the transverse envelope for $U = 0.23$ m/s, shown in Fig. 11, one can clearly see that the structure vibrates in the first mode. In Fig. 13, the velocity $U = 0.38$ m/s, and the predominant mode is the second one. The case for velocity U=0.54 m/s is shown in Fig. 15 and the riser vibrates in the third mode. On the other hand, for velocity $U = 0.85$ m/s, the riser vibrates in the fourth mode. The maximum amplitudes is around $Y/D = 0.65$, and it happens at the second vibration mode.

For a given current, the spectra along the span are similar, indicating the structure oscillates in a preponderant mode. The power spectra shown in Figs. 12, 14, 16, and 18 are for the transverse displacements at section $Z = 25$ m, measured upwards from the sea floor. As the current and the mode of oscillation increases, the observed peak frequency increases. If the reduced velocity and frequency are now defined with the period of the predominant mode, T_n, through the expressions

$$V_r = \frac{UT_n}{D}, \tag{44}$$

$$f_r = \frac{D}{T_n U}, \tag{45}$$

we can summarize the results, and some interesting conclusions can be drawn. The modes of vibration, reduced velocity, and frequency of simulations, for currents varying from 0.16 to 0.93 m/s, are shown in Table 2. The analysis of this table

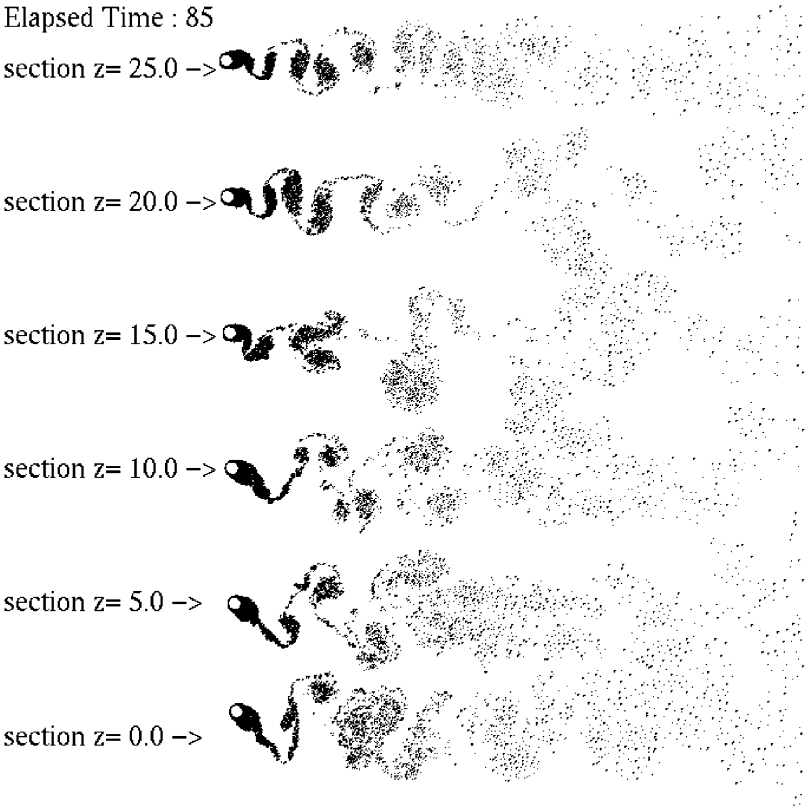

Fig. 8. Wake visualization—reduced velocity $V_r = 9$.

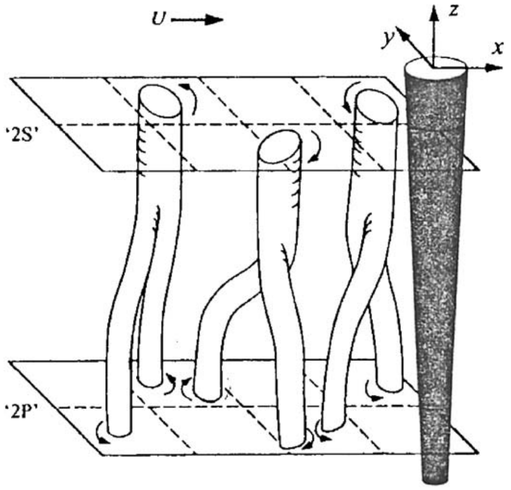

Fig. 9. Hybrid modes 2S to 2P—adapted from Techet et al. (1998).

shows that the selection of mode in which the riser will vibrate occurs in a way to keep the reduced velocity in the range $4 \leqslant V_r \leqslant 7$. The energy transferred from the fluid to the structure is positive in this range of reduced velocity, as Meneghini (1993) has observed. In addition, the reduced frequency lies in the range $0.15 \leqslant f_r \leqslant 0.22$, which is the interval in which lock-in occurs. All these observations corroborate the conclusion that the mode of vibration is characterized solely by the shedding frequency and the interval in which lock-in can occur.

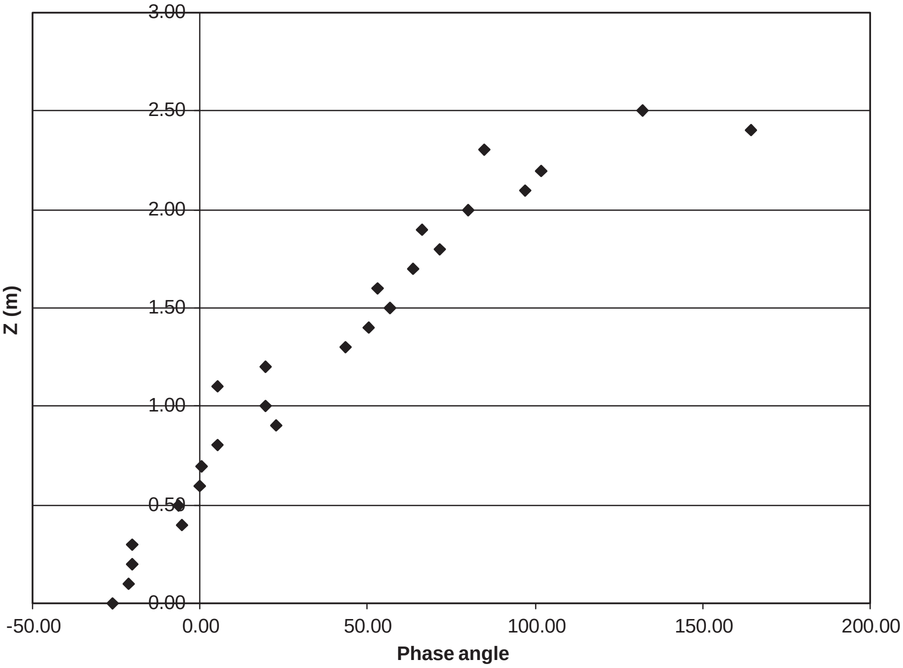

Fig. 10. Phase angle between lift coefficient and cylinder displacement, V_r=5.0.

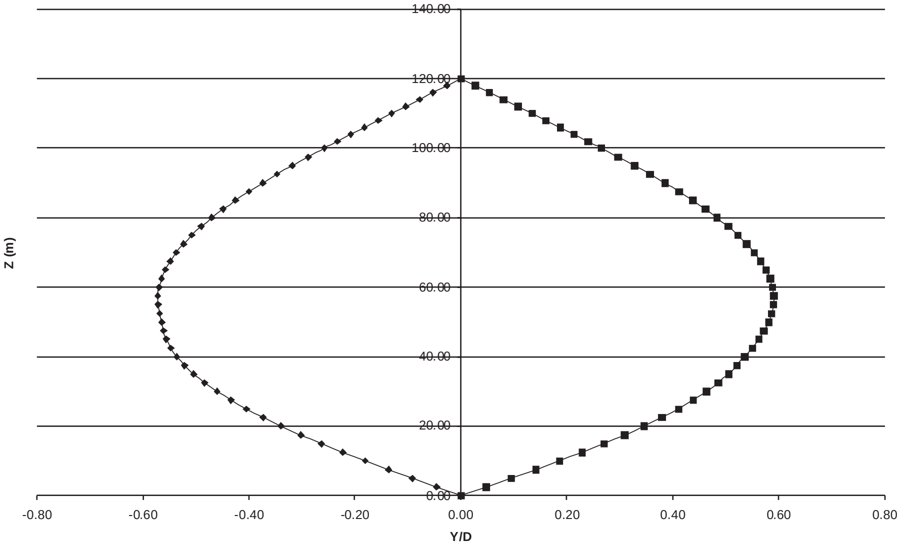

Fig. 11. Transverse envelope, maximum and minimum transverse displacements; U=0.23 m/s, Re = 5.8×10^4.

5. Comparison with quasi-steady theory calculations

The task of validating the calculations of a real riser case is very difficult. There are very few initiatives to measure riser displacements due to vortex-induced vibration. In the present study, we decided to compare the results from the calculations employing the DVM with the results using the quasi-steady theory as described by Ferrari (1998) and Bearman et al. (1984). This model is chosen for the comparison because it employs the same structural model coupled with the CFD calculations presented here. Ferrari employs a more conventional approach to the hydrodynamic force

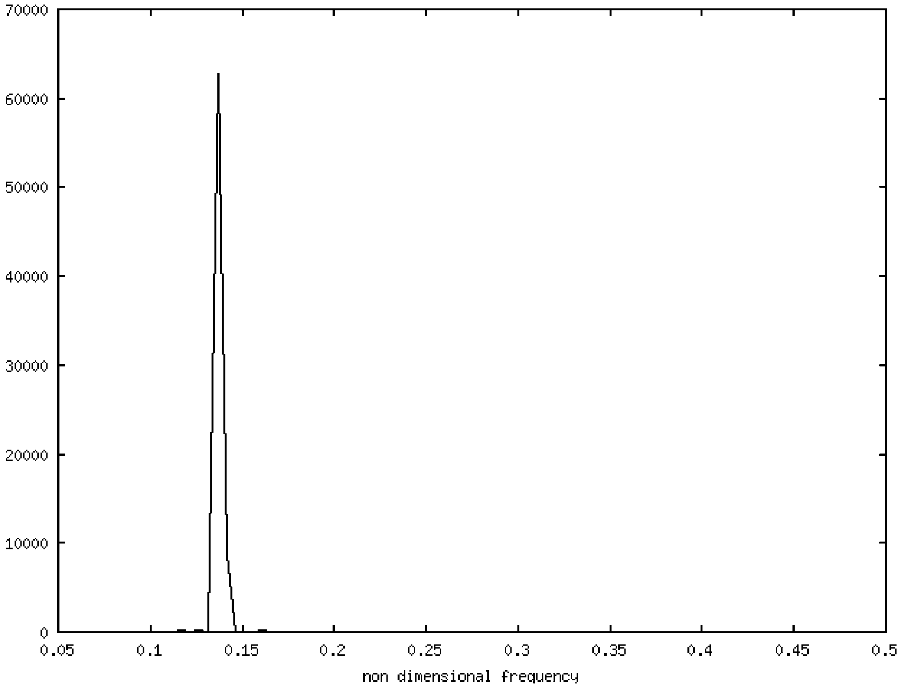

Fig. 12. Power spectrum of the transverse displacements at Z=25.0 m; U=0.23 m/s, Re = 5.8×10^4.

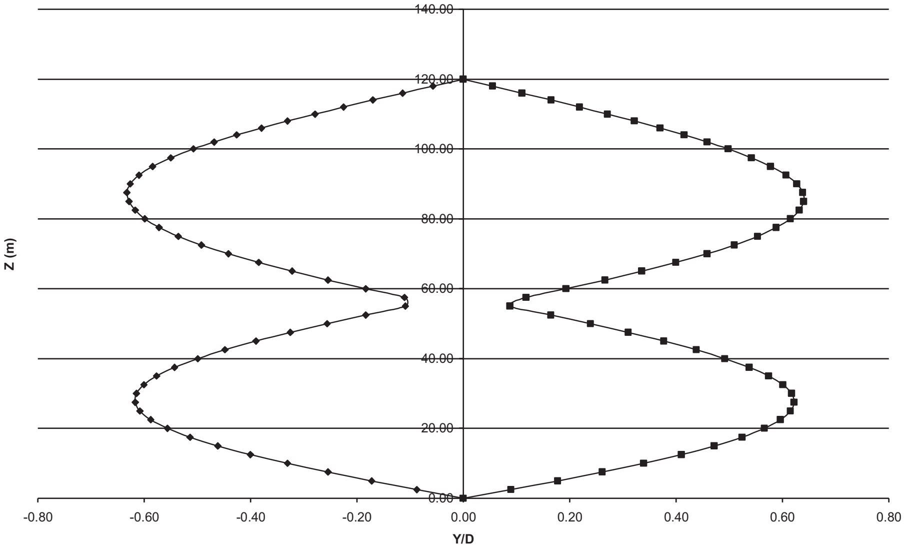

Fig. 13. Transverse envelope, maximum and minimum transverse displacements; U=0.38 m/s, Re = 9.5×10^4.

estimation. In his work, the Morison's equation is utilized to obtain the in line hydrodynamic force. The quasi-steady theory is employed to find the transverse force. More details of his procedure can be found in Ferrari (1998).

The quasi-steady model cannot be applied to the uniform current case since it does not capture the synchronization between the forces and displacements. In the presence of a shear flow, multiple frequencies of vortex shedding take place and a single structural mode does not control the shedding process. With this characteristic in mind, our comparisons with the quasi-steady model are carried out for a shear flow case.

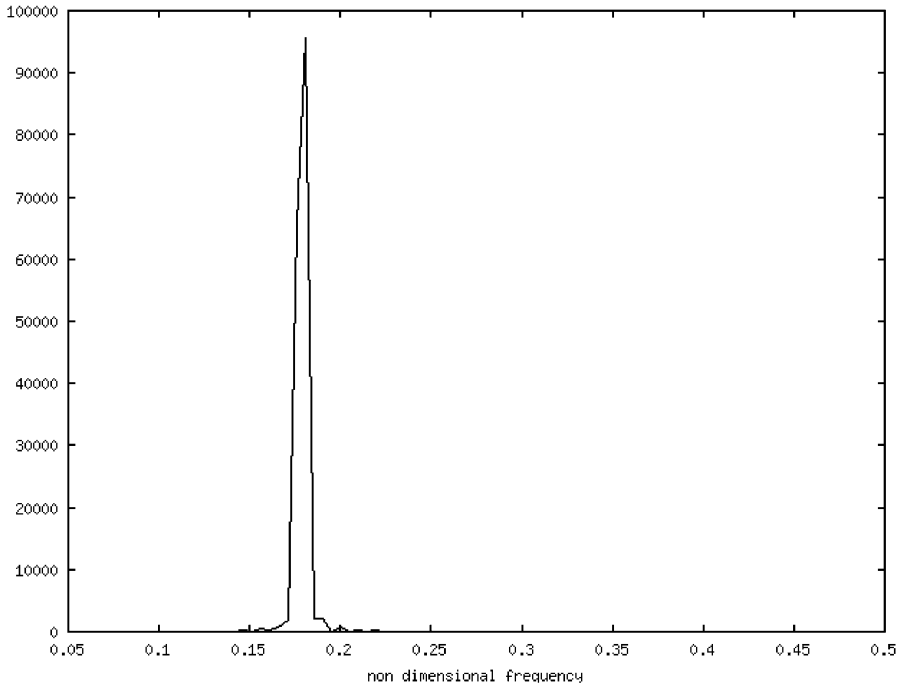

Fig. 14. Power spectrum of the transverse displacements at Z=25.0 m; U=0.38 m/s, Re = 9.5×10^4.

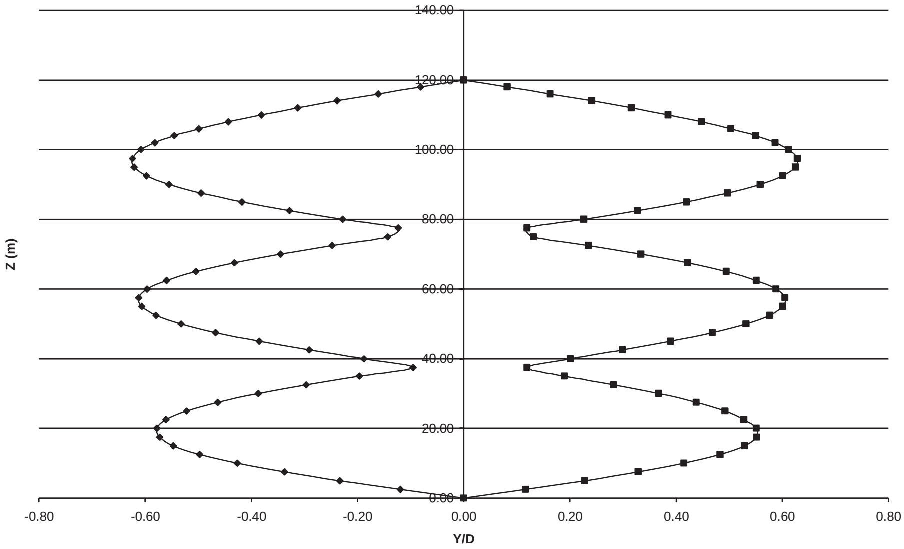

Fig. 15. Transverse envelope, maximum and minimum transverse displacements; U=0.54 m/s, Re = 1.4×10^5.

Two cases are chosen. In both, the current varies linearly along the span. The input parameters employed in the quasi-steady theory calculations are shown below. In the quasi-steady theory model, we must provide the transverse force coefficients, shedding phase, and Strouhal number as parameters for the calculations. The same values as those employed by Ferrari (1998) are used in this paper:

- Force coefficients: drag coefficient, C_d = 1.2; added mass coefficient, $C_A = 0.6$; shedding phase, $\varphi = 20°$; Strouhal number, St = 0.2; transverse force coefficient amplitude, $C_t = 1.2$.

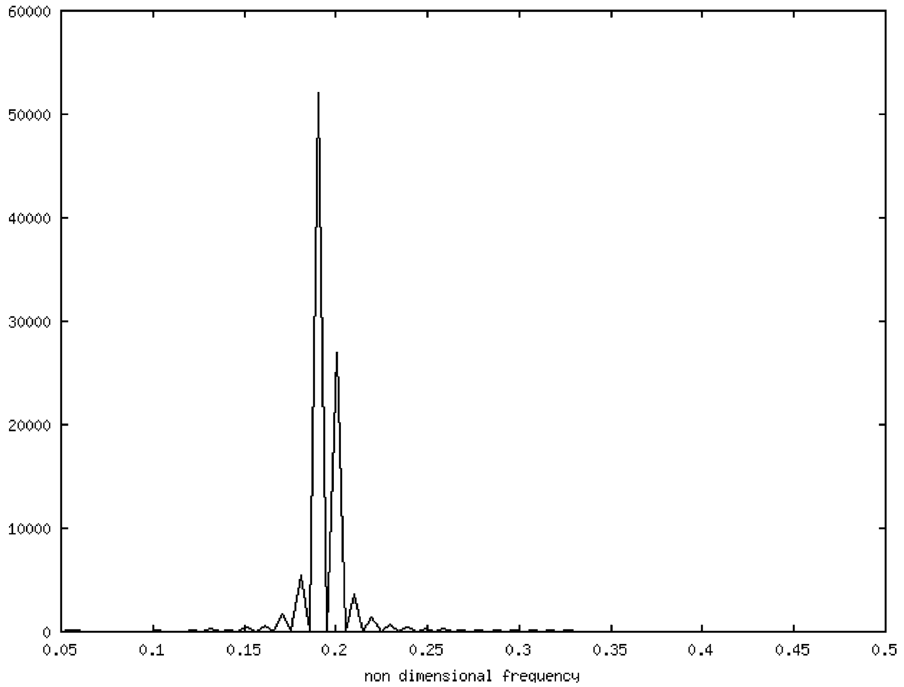

Fig. 16. Power spectrum of the transverse displacements at Z=25.0 m; U=0.54 m/s, $\mathrm{Re} = 1.4 \times 10^5$.

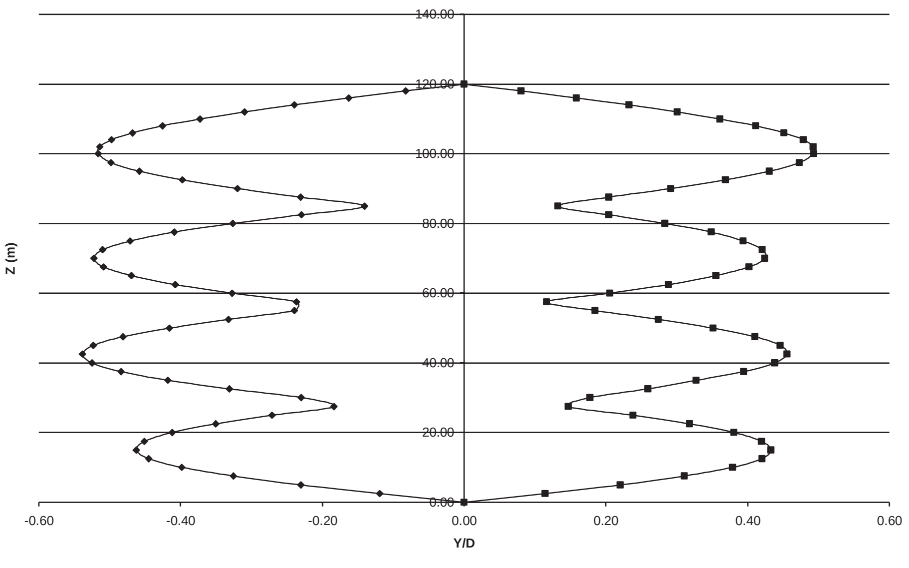

Fig. 17. Transverse envelope, maximum and minimum transverse displacements; U=0.85 m/s, $\mathrm{Re} = 2.1 \times 10^5$.

The structural characteristics of the riser are the same as in the previous section. The riser is modelled with 40 elements equally spaced below the water level and 10 elements, also equally spaced, above the water level. The time step is $\Delta t = 0.05$.

The two shear flows considered for our comparisons vary linearly. In the first case, a trapezoidal current is adopted; the fluid velocity varies from 0.4 m/s at the seabed to 1.2 m/s at the water level. In the second case, a triangular profile is assumed. The velocity at the seabed is 0.4 m/s, at the middle of the riser is 1.2 m/s and at the water level is also 0.4 m/s. Fig. 19 illustrates both cases.

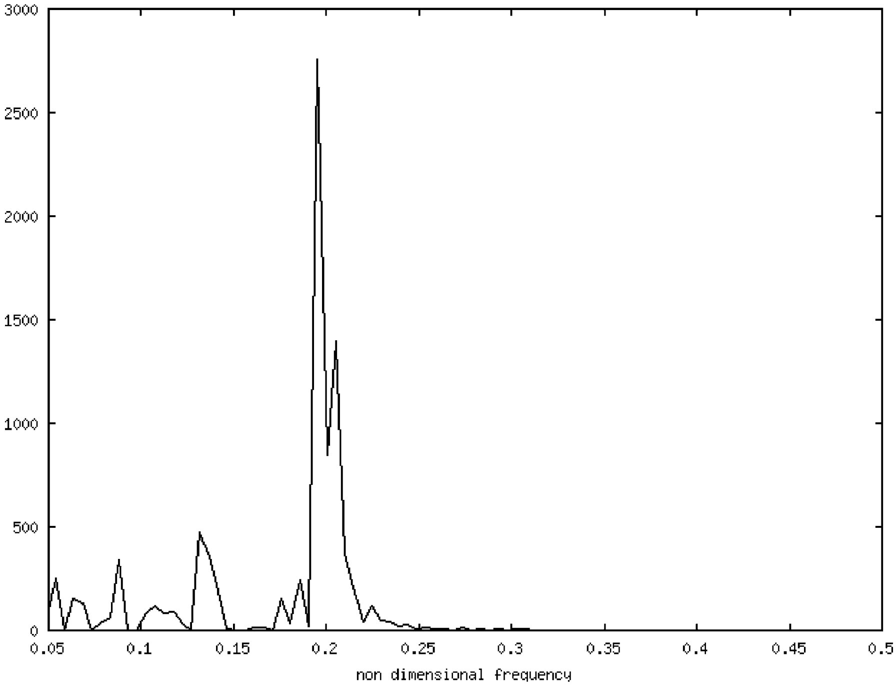

Fig. 18. Power spectrum of the transverse displacements at Z=25.0 m; U=0.85 m/s, Re = 2.1×10^5.

Table 2
Current velocity, vibration mode, reduced velocity, and reduced frequency

U (m/s)	Mode of vibration	Reduced velocity, V_r	Reduced frequency, f_r
0.16	1st	4.51	0.22
0.23	1st	6.76	0.15
0.31	2nd	4.00	0.25
0.38	2nd	4.87	0.20
0.40	2nd	5.14	0.20
0.47	2nd	6.00	0.17
0.54	3rd	4.00	0.25
0.62	3rd	4.57	0.22
0.70	3rd	5.15	0.19
0.78	3rd	5.72	0.17
0.86	4th	4.03	0.25
0.93	4th	4.40	0.23

The maximum and minimum displacement envelopes in the in-line and transverse directions are shown in Figs. 20 and 21, respectively, for Case 1, and Figs. 22 and 23 for Case 2. Comparing the in-line displacement, we can see that the envelopes obtained with the DVM are slight larger than the envelopes obtained with the Morison's equation. It can also be seen that the vibration amplitudes are small. This minor difference is probably due to the drag coefficient adopted in the quasi-steady calculation. The calculations employing the DVM take into account the drag amplification due to the oscillation. The same does not occur with the quasi-steady theory. Comparing the transverse envelope obtained with the DVM and quasi-steady theory, one can notice that the envelopes have similar shapes. We observe that the dominant mode is the fourth one.

The amplitude results obtained with the quasi-steady theory have very small oscillation amplitudes in some particular instants of time. When the oscillation amplitude increases, we notice that the structure vibration changes from the first to the fourth mode. In the results obtained with the DVM, we observe the oscillation changing from the second to the fourth mode. However, these modes appear during shorter periods than those observed with the quasi-steady theory.

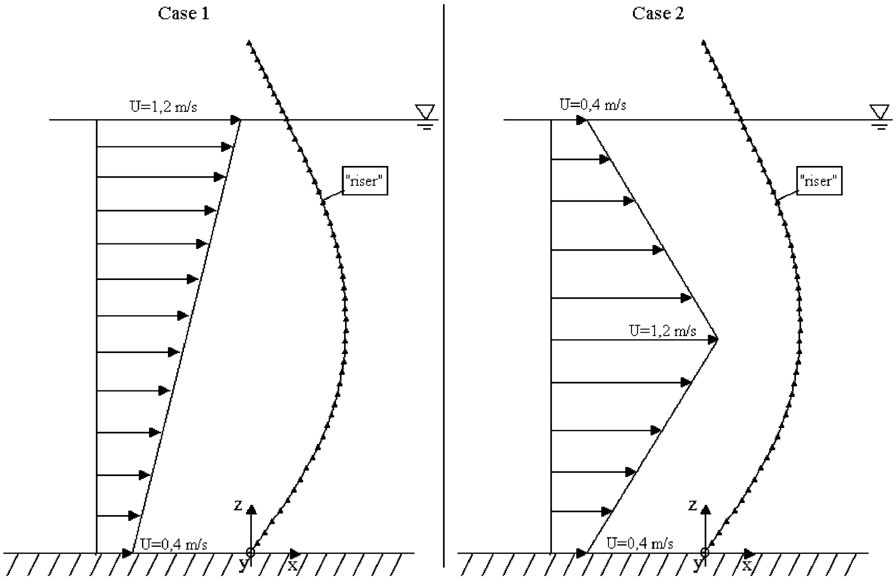

Fig. 19. Shear flow—Cases 1 and 2.

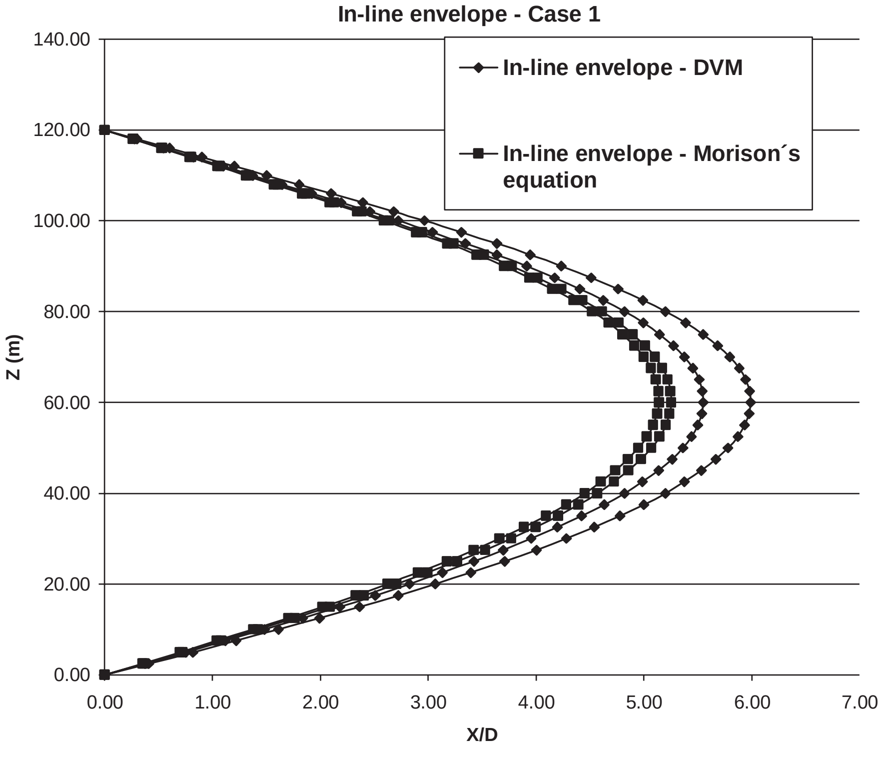

Fig. 20. In-line envelope—Case 1.

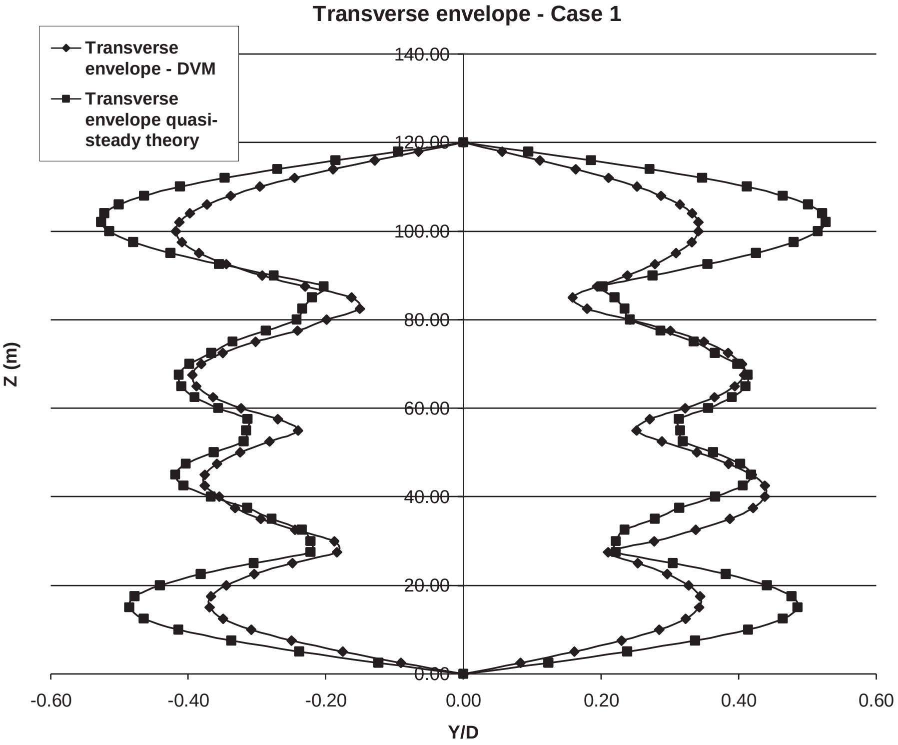

Fig. 21. Transverse envelope—Case 1.

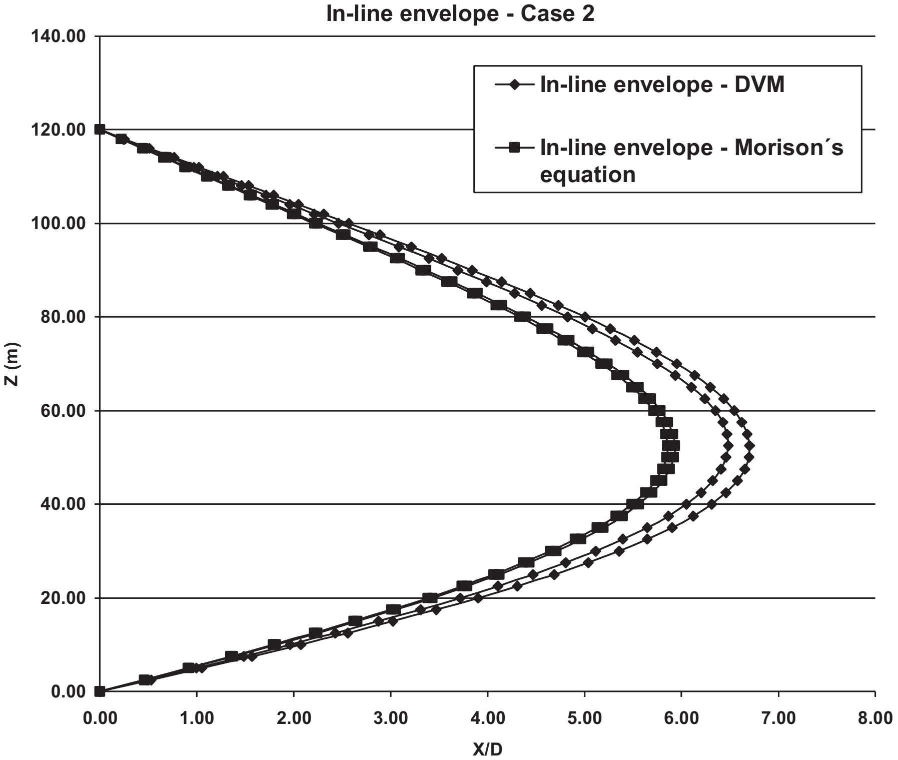

Fig. 22. In line envelope—Case 2.

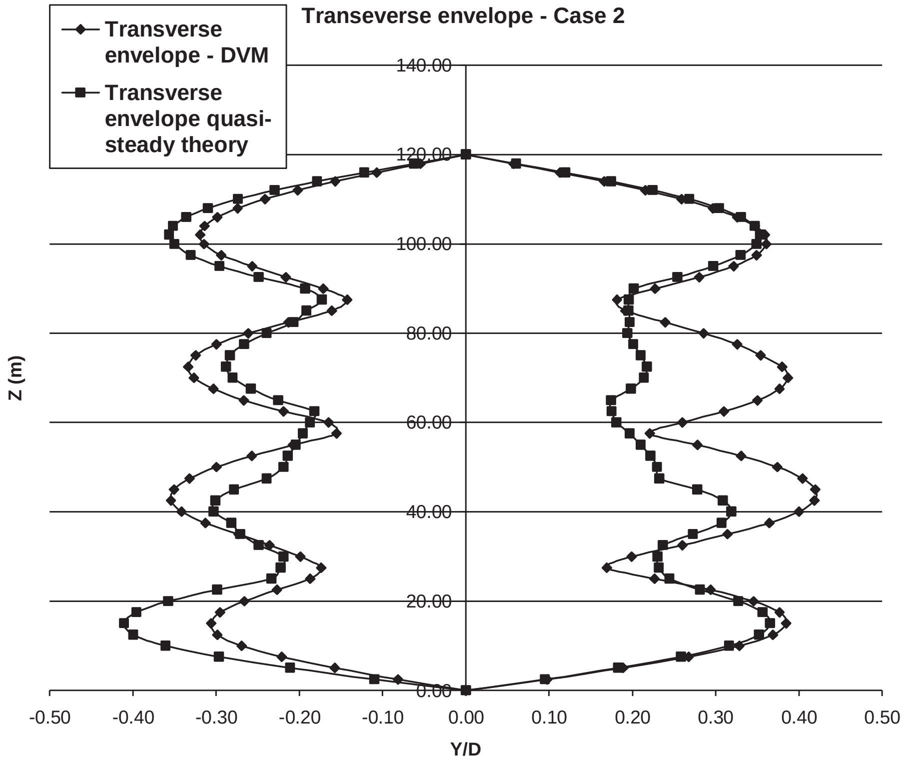

Fig. 23. Transverse envelope—Case 2.

A possible reason for this difference may be that the phase of the transverse force changes along the cylinder length. In the quasi-steady theory, this phase is constant along the cylinder span.

6. Conclusions

Some results of calculations of circular cylinders subject to vortex-induced vibration are shown in this paper. The calculations were compared with experimental results of a flexible cantilever cylinder immersed in an uniform stream. The general trend of the amplitude versus reduced velocity curve obtained with the simulations compares well with the experiments. The only disagreements are related to the maximum amplitude of oscillation and hysteresis. The calculations yield a lower amplitude value than the experimental result. Hysteresis has been observed in the experiments, although the calculations have not shown such a phenomenon. The reason for this disagreement is not clear and it is under investigation, being addressed in a forthcoming paper. The modes of vibration are shown to be directly linked to the reduced velocity range in which the energy transferred from the fluid to the structure is positive. For cases wherein quasi-steady theory is applicable, comparisons have been carried out with this model. The comparisons with the quasi-steady theory give a very good agreement for shear flows.

The main feature of the procedure adopted in this paper is the use of a Lagrangian scheme for the calculation of hydrodynamic force and a three-dimensional scheme for the structural response evaluation. With such an approach, we are able to simulate the flow around risers with no need for mesh interpolations at every time step. The efficient and practical computational tool developed can be employed to investigate the flow around very long cylinders. With such a tool, the study of marine risers installed in very deep water, and subject to vortex-induced vibration, becomes feasible.

Acknowledgements

The authors are grateful to FINEP/CTPetro, FAPESP, CNPq, and PETROBRAS (The Brazilian State Oil Company) for providing them a research grant for this project. The authors also acknowledge José A. P. Aranha, Clóvis A. Martins, Celso P. Pesce, and André L. C. Fujarra for their useful comments regarding our numerical simulations.

References

Bearman, P.W., Graham, J.M.R., Obasaju, E.D., 1984. A model equation for the transverse forces on cylinders in oscillatory flows. Applied Ocean Research 6, 166–172.

Craig, R.R., 1981. Structural Dynamics—An Introduction to Computer Methods. Wiley, New York.

Evangelinos, C., Lucor, D., Karniadakis, G.E., 2000. DNS-derived force distribution on flexible cylinders subject to VIV. Journal of Fluids and Structures 14, 429–440.

Ferrari, J.A., 1998. Hydrodynamic loading and response of offshore risers. Ph.D. Thesis, University of London, UK.

Fregonesi, R.A., 2002. Estudo do escoamento tridimensional ao redor de agrupamento de cilindros em tandem. M.Sc. Dissertation, Escola Politécnica, University of São Paulo, Brazil (in Portuguese).

Fujarra, A.L.C., 1997. Estudo em modelo reduzido de tubo, flexível e liso, submetido ao fenômeno de vibração induzida pela vorticidade. M.Sc. Thesis, Universidade de São Paulo.

Fujarra, A.L.C., Pesce, C.P., Flemming, F., Williamson, C.H.K., 2001. Vortex-induced vibration of a flexible cantilever. Journal of Fluids and Structures 15, 651–658.

Herfjord, K., Larsen, C.M., Furnes, G., Holmås, T., Randa, K., 1999. FSI-simulation of vortex-induced vibration of offshore structures. In: Kvamsdal, T., et al. (Eds.), Computational Methods for Fluid–Structure Interaction. Tapir, Trodheim, pp. 283–303.

Karniadakis, G.E., Sherwin, S., 1999. Spectral/hp Element Method in CFD. Oxford University Press, New York.

Lucor, D., Imas, L., Karniadakis, G.E., 2001. Vortex dislocations and force distribution of long flexible cylinders subjected to shear flows. Journal of Fluids and Structures 15, 641–650.

Meneghini, J.R., 1993. Numerical simulation of bluff body flow control using a discrete vortex method. Ph.D. Thesis, University of London, UK.

Park, W., Higuchi, H., 1989. Computation of flow past single and multiple bluff bodies by a vortex tracing method. Report UMSI 89/88, University of Minnesota Supercomputer Institute, Minnesota, USA.

Patel, M.H., Witz, J.A., 1991. Compliant Offshore Structures. Butterworth-Heinemann, England.

Sarpkaya, T., 1989. Computational methods with vortices—the 1988 freeman scholar lecture. Journal of Fluids Engineering 111, 5–52.

Smith, P.A., Stansby, P.K., 1988. Impulsively started flow around a circular cylinder by the vortex method. Journal of Fluid Mechanics 194, 45–77.

So, R.M.C., Liu, Y., Lai, Y.G., 2003. Mesh shape preservation for flow-induced and vibration problems. Journal of Fluids and Structures 18, 287–304.

Spalart, P.R., Leonard, A., Baganoff, D., 1983. Numerical simulation of separated flows. Ph.D. Thesis, Stanford University, California (NASA).

Techet, A.H., Hover, F.S., Triantafylou, M.S., 1998. Vortical patterns behind a tapered cylinder oscillating transversely to a uniform flow. Journal of Fluids Mechanics 363, 79–96.

Wang, X.Q., So, R.M.C., Liu, Y., 2001. Flow-induced vibration of an Euler–Bernoulli beam. Journal of Sound and Vibration 243, 241–268.

Yamamoto, C.T., 2002. Estudo do escoamento tridimensional ao redor de agrupamento de cilindros lado-a-lado. M.Sc. Dissertation, "Escola Politécnica", University of São Paulo, Brazil (in Portuguese).

Yeung, R.W., Sphaier, S.H., Vaidhyanathan, M., 1993. Unsteady flow about bluff cylinders. International Journal of Offshore and Polar Engineering 3 (2), 81–91.

Zienkiewicz, O.C., Morgan, K., 1983. Finite Elements and Approximation. Wiley, New York.